Monthly Notices of the ROYAL ASTRONOMICAL SOCIETY

MNRAS **459,** 70–83 (2016) doi:10.1093/mnras/stw584
Advance Access publication 2016 March 11

Constraining the efficiency of cosmic ray acceleration by cluster shocks

F. Vazza,[1⋆] M. Brüggen,[1] D. Wittor,[1] C. Gheller,[2] D. Eckert[3] and M. Stubbe[1]

[1]*Hamburger Sternwarte (Hamburg University), Gojenbergsweg 112, D-20535 Hamburg, Germany*
[2]*ETHZ-CSCS, Via Trevano 131, CH-6900 Lugano, Switzerland*
[3]*Astronomy Department, University of Geneva 16, ch. d'Ecogia, CH-1290 Versoix, Switzerland*

Accepted 2016 March 8. Received 2016 March 8; in original form 2016 February 11

ABSTRACT

We study the acceleration of cosmic rays by collisionless structure formation shocks with ENZO grid simulations. Data from the *Fermi* satellite enable the use of galaxy clusters as a testbed for particle acceleration models. Based on advanced cosmological simulations that include different prescriptions for gas and cosmic rays physics, we use the predicted γ-ray emission to constrain the shock acceleration efficiency. We infer that the efficiency must be on average $\leq 10^{-3}$ for cosmic shocks, particularly for the $\mathcal{M} \sim 2-5$ merger shocks that are mostly responsible for the thermalization of the intracluster medium (ICM). These results emerge, both, from non-radiative and radiative runs including feedback from active galactic nuclei, as well as from zoomed resimulations of a cluster resembling MACSJ1752.0+0440. The limit on the acceleration efficiency we report is lower than what has been assumed in the literature so far. Combined with the information from radio emission in clusters, it appears that a revision of the present understanding of shock acceleration in the ICM is unavoidable.

Key words: acceleration of particles – shock waves – intergalactic medium.

1 INTRODUCTION

The growth of cosmic structures naturally leads to the formation of powerful shock waves into the intergalactic and the intracluster medium (IGM and ICM, respectively; e.g. Sunyaev & Zeldovich 1972; Cavaliere & Lapi 2013). The Mach number of shocks within galaxy clusters at late epochs must be low because the mergers are between virialized haloes (Gabici & Blasi 2003). On the contrary, stronger accretion shocks must be located at all epochs in the outer parts of large-scale structures, as they mark the transition from infalling matter to the onset of the virialization process (Miniati et al. 2000; Ryu et al. 2003). Cosmological simulations show that the bulk of kinetic energy dissipation in the cosmological volume proceeds via shocks with Mach numbers $2 \leq \mathcal{M} \leq 3$ (e.g. Vazza et al. 2011).

Radio relics are steep-spectrum radio sources that are usually detected in the outer parts of galaxy clusters, ∼0.5–3 Mpc from their centres and often found in clusters with a perturbed dynamical state e.g. Ensslin et al. (1998) and Hoeft & Brüggen (2007). However, radio observations of radio relics (Ferrari et al. 2008; Feretti et al. 2012) are biased towards merger shocks with $2 \leq \mathcal{M} \leq 5$, due to the larger weighting of radio-emitting electrons with a flatter spectral index (Skillman et al. 2013; Hong et al. 2014). Diffusive shock acceleration (DSA; Caprioli e.g. 2012; Kang & Ryu e.g. 2013; Caprioli & Spitkovsky e.g. 2014a) has been singled out as the most likely mechanism to accelerate relativistic particles at cosmic collisionless shocks. However, the relative efficiency of this process for electrons and protons, and its dependence on the shock and plasma parameters are poorly constrained. Recently, hybrid simulations have shown that the DSA of relativistic protons and the cosmic ray (CR)-driven amplification of magnetic fields in $5 \leq \mathcal{M} \leq 50$ shocks are efficient only for quasi-parallel configurations, $\theta \leq 45^{\circ}$ (Caprioli & Spitkovsky 2014a).

While the power-law emission spectra of radio-emitting electrons in radio relics are naturally explained by DSA (e.g. Hoeft & Brüggen 2007; van Weeren et al. 2010), recent modelling suggests that at least in some cases the measured acceleration of electrons is too large, and at odds with DSA (e.g. Kang, Ryu & Jones 2012; Pinzke, Oh & Pfrommer 2013). The inclusion of re-accelerated particles can alleviate the tension in some cases, yet in order for the CR protons to be equally reaccelerated and become detectable in γ-rays, their injection efficiency must be much below the predictions from DSA (Brunetti & Jones 2014; Vazza & Brüggen 2014; Vazza et al. 2015).

Our findings suggest that additional acceleration mechanisms might be responsible for channelling energy into the acceleration of radio-emitting electrons, while keeping the acceleration efficiency of protons rather low. Promising results in this direction have been recently obtained with particle-in-cell simulations (Guo, Sironi & Narayan 2014a,b).

The release of relativistic protons into the ICM by cosmological shock waves, and the fact that they can be stored there for longer than the Hubble time has been investigated in many works (Dennison 1980; Berezinsky, Blasi & Ptuskin 1997; Blasi & Colafrancesco 1999; Pfrommer et al. 2007). Interactions with the thermal ions of the ICM lead to diffuse hadronic γ-ray emission, in the range

⋆ E-mail: franco.vazza@hs.uni-hamburg.de

Table 1. List of the simulations used in this work. Column 1: size of the simulated volume. Column 2: number of grid cells. Column 3: spatial resolution. Column 4: physical implementations and run name. Column 5: DSA efficiency of CRs (KJ07 = Kang & Jones 2007, KR13 = Kang & Ryu 2013, 10^{-3} = constant efficiency, CS14 = Caprioli & Spitkovsky 2014a).

$L_{\rm box}$	$N_{\rm grid}$	Δx	Details	DSA-efficiency
216 Mpc h^{-1}	2048^3	105 kpc h^{-1}	CUR1 non-rad.	KR13
108 Mpc h^{-1}	1024^3	105 kpc h^{-1}	CUR2 non-rad.	KR13
108 Mpc h^{-1}	1024^3	105 kpc h^{-1}	CUR2 non-rad.	KJ07
108 Mpc h^{-1}	1024^3	105 kpc h^{-1}	CUR2 cool.+AGN(high)	KR13
108 Mpc h^{-1}	1024^3	105 kpc h^{-1}	CUR2 cool.+AGN(low)	KR13
108 Mpc h^{-1}	1024^3	105 kpc h^{-1}	CUR2 non-rad.	10^{-3}
108 Mpc h^{-1}	1024^3	105 kpc h^{-1}	CUR2 cool.+AGN(low)	10^{-3}
108 Mpc h^{-1}	1024^3	105 kpc h^{-1}	CUR2 non-rad.	CS14

of what can already be tested by γ-ray observations (Aharonian et al. 2009; Ackermann et al. 2010; Aleksić et al. 2010, 2012; Arlen et al. 2012; The Fermi-LAT Collaboration et al. 2014; Zandanel & Ando 2014). To date, no diffuse γ-ray emission from the ICM has been detected by *Fermi* (Ackermann et al. 2010; The Fermi-LAT Collaboration et al. 2014). With this information, one can set upper limits on the amount of CR-protons in the ICM, of the order of a few per cent for the virial volume of clusters provided that the radial distributions are similar to that of thermal baryons (Ackermann et al. 2010; Huber et al. 2013; Griffin, Dai & Kochanek 2014; Zandanel & Ando 2014).

In this work, we analyse a large sample of simulated galaxy clusters and compare the expected level of hadronic γ-ray emission as a function of the assumed acceleration scenario to constraints from observations.

2 METHODS

Our simulations are produced using original modifications for CR physics on top of the ENZO code (Bryan et al. 2014), as presented in previous work (Vazza et al. 2012; Vazza, Brüggen & Gheller 2013; Vazza, Gheller & Brüggen 2014a). We assume the *Wilkinson Microwave Anisotropy Probe* 7-yr cosmology (Komatsu et al. 2011) with $\Omega_0 = 1.0$, $\Omega_{\rm B} = 0.0455$, $\Omega_{\rm DM} = 0.2265$, $\Omega_\Lambda = 0.728$, Hubble parameter $h = 0.702$, a normalization for the primordial density power spectrum $\sigma_8 = 0.81$ and a spectral index of $n_{\rm s} = 0.961$ for the primordial spectrum of initial matter fluctuations, starting the runs at $z_{\rm in} = 30$.

Compared to the suite of simulations presented in Vazza et al. (2014a) here, we only analyse boxes of 300^3 and 150^3 Mpc^3 simulated with 2048^3 and 1024^3 cells DM^{-1} particles, respectively. In the second case, several resimulations compare the effects of CRs and gas physics on the hadronic emission. The use of large grids with constant resolution yields a large sample of clusters with appropriate detail in describing the outer cluster regions, where most shocks occur (Vazza et al. 2011). A study of resolution effects is provided in the appendix.

Table 1 gives a schematic view of the runs used in this work. All haloes with $\geq 10^{13}$ M$_\odot$ are sampled by at least $\sim 10^4$ dark matter (DM) particles, ensuring a robust modelling of the innermost cluster dynamics. At $z = 0$, the CUR1 box contains $\approx$170 haloes with masses $M_{\rm v} \geq 10^{13}$ M$_\odot$ and $\approx$400 with masses $M_{\rm v} \geq 10^{14}$ M$_\odot$ while the CUR2 boxes contains about $\sim$8 fewer objects due to their smaller volume. Although our goal of properly resolving the injection of CRs in a large sample of galaxy cluster can only be presently achieved with large unigrid runs, in Section 3.4 we also discuss higher resolution simulations of a galaxy cluster where we used adaptive mesh refinement (AMR), in order to better compare with small-scales X-ray and radio features of an observed galaxy cluster.

2.1 CR physics

The injection of CRs and their dynamical feedback on the evolution of baryons is incorporated into the PPM hydrodynamical method of ENZO, using a two-fluid approach (Vazza et al. 2012, 2014a). The efficiency of conversion between the shock kinetic energy flux and the CR-energy flux is set by the Mach number measured on-the-fly. The models of DSA tested in these simulations follow from modelling of shock acceleration with 1D diffusion-convection methods (e.g. Kang & Jones 2007; Kang & Ryu 2013). Following these results, we assume that a fraction η of the kinetic energy flux across the shocks surface ($\Phi_{\rm kin}$) is converted into CR-energy: $\Phi_{\rm CR} = \eta(\mathcal{M})\Phi_{\rm kin}$, where $\eta = \eta(\mathcal{M})$. Simulated shocks can both inject CRs and re-accelerate pre-existing CRs, and we model both processes at run-time by appropriately rescaling the efficiency function as a function of the energy ratio between CR and gas upstream of each shock (Vazza et al. 2014a). Away from shocks, the CR-fluid is advected using the fluxes from the PPM solver, assuming that CRs are frozen into the gas component by magnetic fields, which is realistic given the large time-scale for CRs diffusing out of our $\geq$100 kpc cells. The dynamical impact of CRs follows from the effective equation of state of each cell, which comes from the energy-weighted ratio of the gas and CRs ultrarelativistic index, $4/3 \leq \Gamma_{\rm eff} \leq 5/3$. We also include Coulomb and hadronic losses for CRs based on Guo & Oh (2008).

In this work, we tested the acceleration efficiency by Kang & Jones (2007), the (less efficient) acceleration scenario by Kang & Ryu (2013) and a more simplistic scenario with a fixed acceleration efficiency of $\eta = 10^{-3}$ independent of the Mach number. We have also tested the more recent studies of DSA with hybrid simulations by Caprioli & Spitkovsky (2014a). In the absence of an analytical or interpolated prescription for the acceleration efficiency as a function of Mach number and shock obliquity (which would require an expensive exploration of parameters), we can roughly model the net DSA acceleration efficiency of this model by rescaling the efficiencies of the Kang & Ryu (2013) model for an appropriate constant. The acceleration efficiency measured by Caprioli & Spitkovsky (2014a) for $\mathcal{M} \sim 5-10$ quasi-parallel shocks is $\approx$0.5 of the efficiency in Kang & Ryu (2013) for the same Mach number range. If we assume the probability distribution of shock obliquities to be purely random ($P(\theta) \propto \sin(\theta)$), only $\approx$0.3 of shocks have $\theta \leq 45^\circ$. Hence, by combining these two factors we can roughly mimic the effect of DSA in the model by Caprioli & Spitkovsky (2014a) by rescaling the Kang & Ryu (2013) acceleration model by $f_{\rm CS} = 0.15$. Obviously, this is a very crude assumption and we defer to future magnetohydrodynamical simulations to study how the shock obliquity affects the injection of CRs (Wittor et al., in preparation).

2.2 Gas physics

In runs including radiative cooling of gas, we assume a constant composition of a fully ionized H–He plasma with a uniform metallicity of $Z = 0.3\,Z_\odot$. The APEC emission model (e.g. Smith et al. 2001) has been adopted to compute the cooling function of each cell at run-time as a function of temperature and gas density (Bryan et al. 2014). For the cold gas in the simulated volume, with temperatures $T \leq 10^4$ K, we use the cooling curve of Smith et al. (2011),

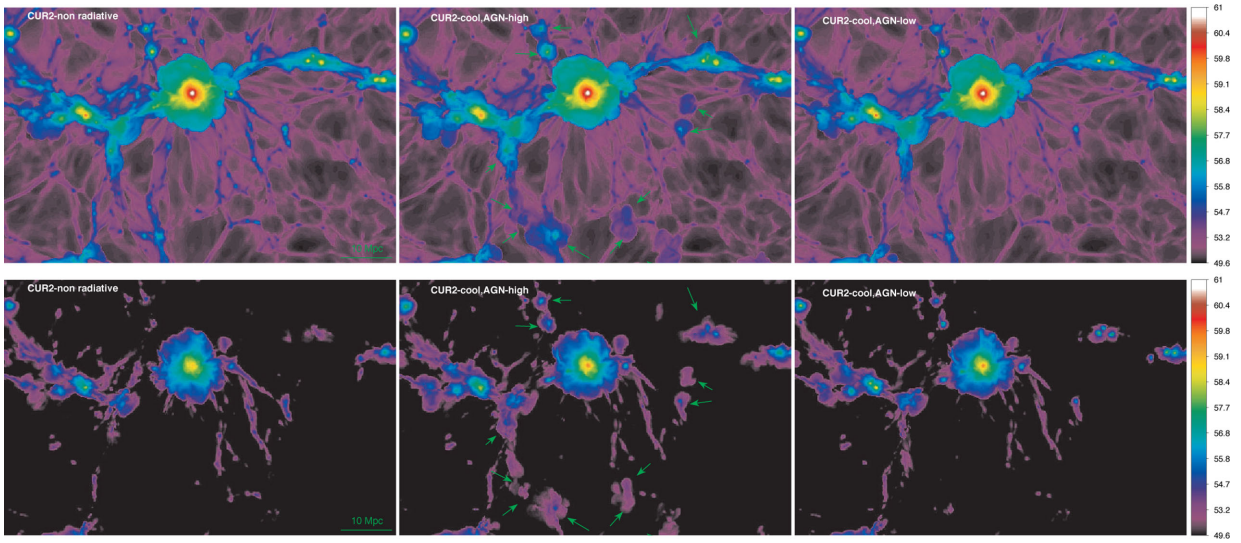

Figure 1. Two-dimensional slice (with thickness 3 Mpc) of the gas energy (top panels) and CR-energy (bottom panels) for a subvolume of the CUR2 volume at $z = 0$, where we compare the non-radiative and the cooling plus AGN feedback runs. The colour bar gives the energy per cell in units of $\log_{10}$ [erg]. To guide the eye, we indicate with green arrows the regions where the effect of AGN feedback is more prominent.

which is derived from a complete set of metals (up to an atomic number 30), obtained with the chemical network of the photoionization software CLOUDY (Ferland et al. 1998). The thermal effect of the UV re-ionization background (Haardt & Madau 1996) is approximately modelled with a gas temperature floor within $4 \leq z \leq 7$ (Vazza et al. 2010). The implementation of feedback from AGN has been presented in Vazza et al. (2013, 2014a). The code releases bipolar thermal jets at high gas density peaks in the simulation, identified within all massive haloes. Our feedback scheme starts at $z = 4$ ('AGN' model) or at a lower redshift, $z = 1$ ('AGN-low' model) and deposits $E_{\rm AGN} = 10^{59}$ erg of thermal energy in the two cells on opposite sides of the gas density peaks (tagged as $n \geq n_{\rm AGN} = 10^{-2}$ cm^{-3} comoving), with a random direction along the coordinate axes of the grid. This method for AGN feedback is admittedly simplistic as it by-passes, both, the problem of monitoring the mass accretion rate on to the central black hole within each galaxy, and the complex small-scale physical processes which couple the energy from the black hole to the surrounding gas (see discussion in Vazza et al. 2014a). However, the tests presented in this work (Section 3.1) show it can produce realistic profiles of clusters on $\geq$100 kpc scales.

2.3 AMR resimulations of MACSJ1752.0+0440

We have performed an additional AMR resimulation of one massive galaxy cluster that shows a good X-ray and radio morphological similarity with the cluster MACSJ1752.0+0440, that we already studied in Bonafede et al. (2012). Similar to other clusters with double relics, this object represents an important testbed for particle acceleration in the ICM, because the location of relics allows us to precisely constrain the timing and the parameters of the merger (Vazza & Brüggen 2014; Vazza et al. 2015). This cluster has a total virial mass of $\approx 1.37 \times 10^{15}$ M$_\odot$ at $z = 0$, while this is $\approx 0.65 \times 10^{15}$ M$_\odot$ at the epoch of a major merger at $z = 0.3$, similar to what is inferred from the X-ray data of MACSJ1752.0+0440 at $z = 0.366$. We produced multiple resimulations of this object by varying the modelling of CR injection and use the *Fermi* data to constrain the CR-acceleration scenario. The initial conditions for this object are taken from set of nested grids sampling a volume of 264^3 Mpc^3, centred on the formation region of the cluster. AMR based on the local gas/DM overdensity and on velocity jumps is used to increase the resolution in the cluster region additional 2^3 times, down to a maximum resolution of $\approx$25 kpc h^{-1} for a $\sim$80 per cent fraction of the ICM volume. For more details on the simulation procedure, we refer the reader to Vazza et al. (2010).

2.4 γ-ray observation of MACSJ1752.0+0440

For this project, we derived upper limits for the γ-ray emission from the region of MACSJ1752.0+0440 at $z = 0.366$, analysing the *Fermi* catalogue.

We analysed the data of the Large Area Telescope (LAT) on board *Fermi* at the position of MACS J1752 to set constraints on the π^0 emission arising from the interaction of CR protons with the ambient ICM. We follow the method presented in Vazza et al. (2015) to analyse the *Fermi*-LAT data. Namely, we use the SCIENCETOOLS v9r32p5 software package and the P7SOURCE_V6 instrument response files. We construct a model for the expected γ-ray spectrum arising from π^0 decay by convolving the simulated CR spectrum in the [0.2–300] GeV band with the proton–proton interaction cross-section from Kelner, Aharonian & Bugayov (2006). The observed spectrum is then fitted with the model template and the significance of the signal over the background is estimated by computing the likelihood ratio between the best-fitting model and the null hypothesis (i.e. no additional source), usually referred to as the test statistic (TS). This analysis yields a very mild improvement in the likelihood (TS = 0.04), which indicates that no significant signal is detected at the position of MACS J1752. The 95 per cent upper limit to the source flux is 1.2×10^{-9} photons cm^{-2} s^{-1} in the [0.2–300] GeV band. For more details on the data analysis procedure, we refer to Huber et al. (2012, 2013).

3 RESULTS

3.1 Cluster properties

The panels in Fig. 1 show the thermal and CR energy distribution in a subvolume of the CUR2 run with different prescriptions for gas

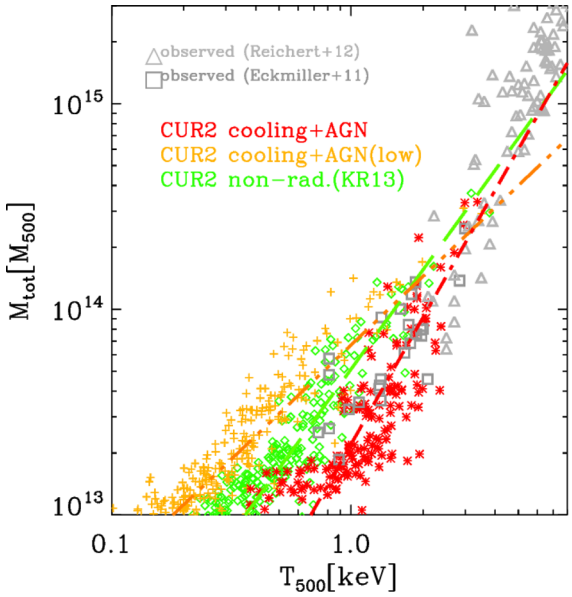

Figure 2. Mass–temperature scaling relation for the haloes in the radiative and non-radiative runs of the CUR2 volume (150^3 Mpc^3), computed inside R_{500} for each object at $z = 0$. The additional lines show the best fit of the simulated data, while the two set of grey symbols are for real cluster observations using *Chandra* by Eckmiller, Hudson & Reiprich (2011) and Reichert et al. (2011). To better compare with the simulated cluster and minimize the effect of cosmic evolution, we only consider observed cluster in the $0 \leq z \leq 0.2$ redshift range.

physics and containing clusters of different masses. The impact of gas cooling and feedback is not very significant on the scale of the two massive objects in this image ($\sim 2 \times 10^{14}$ and $\sim 4 \times 10^{14}$ M$_\odot$, respectively), while it is more evident at the scale of galaxy groups, where AGN feedback promoted the expulsion of entropy and CR enriched gas outside of haloes, as an effect of past powerful bursts. Compared to the non-radiative case, the core of clusters/groups is always richer of CRs, due to additional injection following the shocks released by the thermal AGN feedback. The CR energy is everywhere smaller than the gas energy, with a ratio that goes from a few per cent to a few tens of percent going from the centre to the outskirts of clusters. In the lower redshift AGN feedback case, the outer atmosphere of clusters is less extended in the other cases, due to the unbalanced compression by cooling.

In order to assess how realistic the thermal gas distribution in our clusters is, we compute the mass–temperature relation for all identified haloes in the volume, inside the reference overdensity of $\Delta = 500$, and compare it to the X-ray observed scaling relations by Reichert et al. (2011) and Eckmiller et al. (2011), see Fig. 2.

As expected, clusters in non-radiative runs closely follow the self-similar scaling, $M \propto T^{3/2}$, while the cooling+AGN runs show significant departures from self-similarity. The run with lower redshift AGN feedback produces significant overcooling in small-size haloes, which produces a *flattening* of the (T, M) relation. In these runs the AGN feedback is just sufficient to quench the cooling flow, but most clusters below $M_{500} \leq 10^{14}$ M$_\odot$ are too cold compared to observations. On the other hand, the run with early AGN feedback produce a scaling relation which is in better agreement with observations, with hints of a steepening for $M_{500} \leq 10^{14}$ M$_\odot$. No objects with a central temperature below $\sim$0.5 keV are formed in this case. The scatter in temperature is also increased due to the intermittent AGN activity.

We conclude that our fiducial AGN model is suitable to produce clusters with a realistic mass–temperature (and hence gas energy) relation, and can therefore represent a robust baseline model to test the outcome of different CR-acceleration models against *Fermi* data. However, the lack of spatial resolution and physics at the scale of galaxies in these runs makes it impossible to model star formation and star feedback (both energetic and chemical), and to properly compare the outcome of this against observed relations (see e.g. Planelles & Quilis 2013; Hahn et al. 2015; Rasia et al. 2015, for recent reviews). In the appendix (Section B), we also show that the impact of CRs on the X-ray scaling relations is negligible in both tested acceleration models.

In Fig. 3, we show the average radial profiles of gas temperature and density for our clusters, for the CUR1 and the CUR2 run with cooling and high-redshift AGN feedback. The results are compared to the observed mean profiles of gas density and temperature (Eckert et al. 2012) and pressure (Planck Collaboration V 2013) derived from X-ray and SZ observations of nearby clusters (Eckert et al. 2012; Planck Collaboration V 2013). Observations reported the consistent detection of a bimodal gas distribution in clusters having a cool-core (CC) or a without it (NCC), which shows up prominently as a difference of the innermost density, temperature and entropy profiles (e.g. De Grandi & Molendi 2001; Cavagnolo et al. 2009; Hudson et al. 2010) as well as a smaller large-scale radius difference in density (Eckert et al. 2012).

We therefore split our cluster samples into CC and NCC classes based on the central temperature gradient observed in each object at $z = 0$. This is one of the several possible working definitions proposed in the literature (e.g. Hudson et al. 2010), which work well for the coarse resolution we have for the central regions of the lowest mass systems in the sample. The gradient is defined as $\Delta T = T(r + \Delta r) - T(r)$ based on the spherical mass-weighted temperature profile, $T(r)$, and we consider a cluster CC-like if $\Delta T \geq 0$ in the first radial bin, or NCC-like otherwise.

All objects with $M_{\rm vir} \geq 5 \times 10^{13}$ M$_\odot$ of the non-radiative CUR1 data set are considered as NCC according to this criterion. In the CUR2 sample with cooling and low-redshift feedback case, we find an NCC/CC ratio close to 0.5, yet all our objects are characterized by a too large central density, similar to or exceeding the one of CC systems. On the other hand, with the adoption of cooling and efficient feedback the ratio becomes NCC/CC $\sim$ 0.32, i.e. quite close to observations (i.e. $\approx$0.39; Hudson et al. 2010).

While the gas density profiles of clusters with different masses can be averaged, in averaging the temperature profiles we normalized each profile at R_{500}, based on the self-similar $T_{500} \propto M_{500}^3/2$ relation (e.g. Eckert et al. 2013). The large-scale trends of thermodynamical quantities are reproduced reasonably well by our runs. The cluster population in the CUR1 non-radiative run present an overall good match of the observed profiles in the range $0.1 \leq R/R_{\rm vir} \leq 0.9$, but cannot reproduce the CC/NCC bimodality. The cluster population of the CUR2 run with cooling and early feedback does a similarly good job and shows hints of the CC/NCC bimodality. However, in this case the innermost density/pressure profile is underestimated compared to observations, due to the fact that the average cluster mass in this smaller volume is smaller and an increasing ratio of clusters has a core which is relatively poorly resolved compared to the CUR1 run, where many larger clusters are formed. We stress that while this effect may cause an underestimate of the hadronic γ-ray emission from the innermost regions (as this scales as $\propto n^2$), the effect is overall not large because typically only $\leq$10 per cent of the γ-emission is produced within $\leq 0.1 R_{\rm vir}$ (see Section A2). On the other hand, the cluster population in the

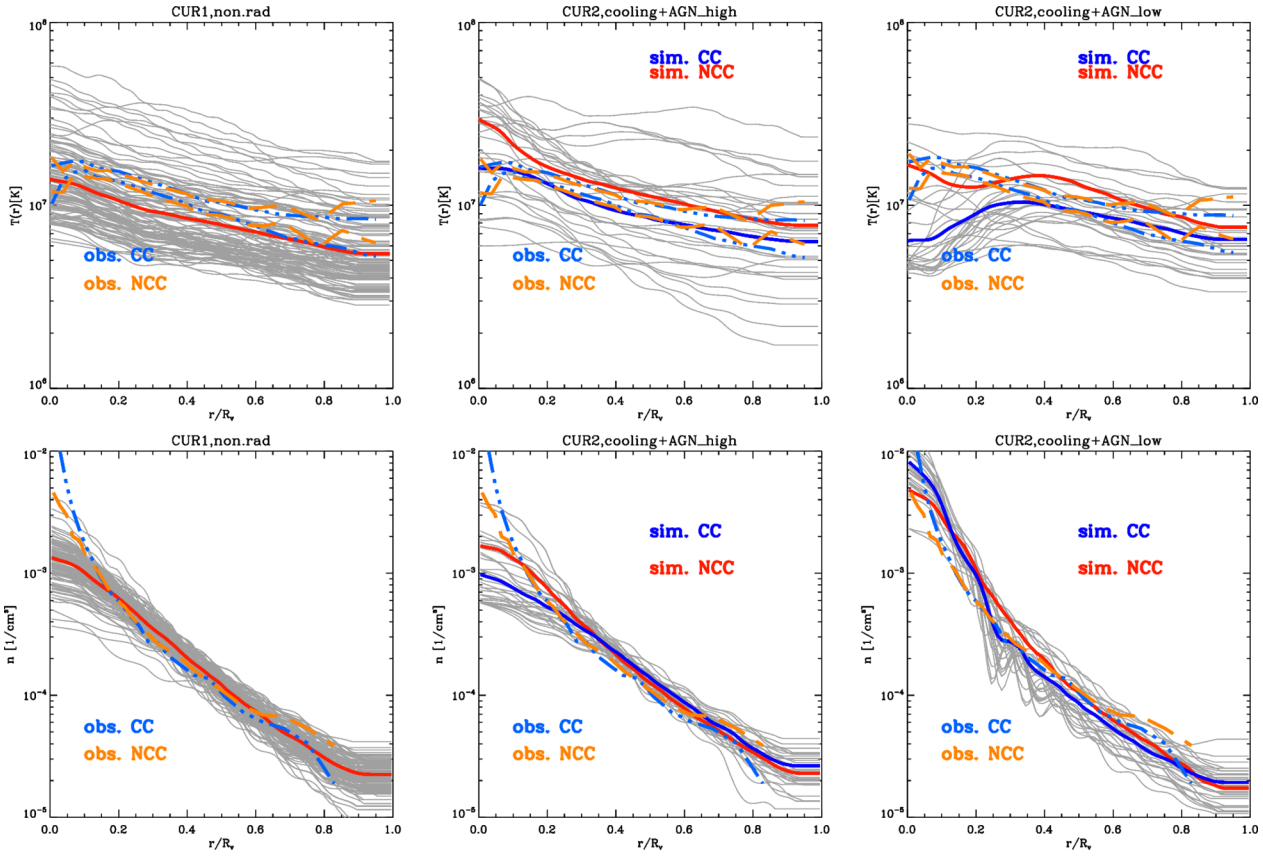

Figure 3. Radial profile of gas temperature and density for all simulated clusters with $M_{\rm vir} \geq 10^{14}\,{\rm M}_{\odot}$ in the $300^3\,{\rm Mpc}^3$ volume of the CUR1 run (non-radiative) and in the $150^3\,{\rm Mpc}^3$ volume of the CUR2 run (with cooling and two AGN feedback modes). The profiles of individual objects are shown in grey, while the $\pm\sigma$ around the mean profile of the sample are drawn with continuous lines (red lines for the NCC-like, blue line for the CC-like or the non-radiative clusters). The additional lines shows the $\pm\sigma$ around the mean profile of CC (dashed light blue) or the NCC (dot–dashed orange) from observations (Eckert et al. 2012; Planck Collaboration V 2013).

CUR2 run with low-redshift feedback produces typically too cold and dense CC clusters compared to observations, as an effect of overcooling.

In summary, the comparison with observations suggests that the clusters in the non-radiative CUR1 run as well as in the cooling+AGN CUR2 run can be further used to study CR acceleration. These cluster populations are representative enough of the global ICM properties for a wide range of masses/temperature to allow a comparison with *Fermi* observations in a similar range of masses. In particular, while clusters in the CUR1 can best represent the high-mass end of the observed distribution ($\geq 5 \times 10^{14}\,{\rm M}_{\odot}$), the clusters in the CUR2 run can be used to better study the CC and NCC populations in the lower mass end.

3.2 CR properties

We extracted the spatial distribution of CR-energy for each simulated cluster at $z = 0$, and estimate the relative pressure ratio of CRs compared to the thermal gas pressure. This is computed by integrating the total pressure of CRs within increasing radii, and dividing this by the total gas pressure within the same radius, $X(R) = P_{\rm cr}(<R)/P_{\rm g}(<R)$. The pressure of CRs is $P_{\rm CR} = (\Gamma_{\rm CR} - 1)E_{\rm CR}$, where $E_{\rm CR}$ is the primitive variable simulated with our two-fluid method (Section 2.1). We consider the ultrarelativistic equation of state for CRs, $\Gamma_{\rm CR} = 4/3$, and therefore the pressure ratio can be written as $X = P_{\rm CR}/P_{\rm g} = [(\Gamma_{\rm CR} - 1)/(\Gamma - 1)]E_{\rm CR}/E_{\rm g} = 0.5E_{\rm CR}/E_{\rm g}$.

The panels of Fig. 4 give the profiles of $X(R)$ of the simulated clusters at $z = 0$, Here, we limit to the CUR1 run and to the CUR2 radiative run with high-redshift AGN feedback, where we further split the sample into CC-like and NCC-like objects. The average profiles are always very flat up to the virial radius, and are well fitted by a second-order polynomial,

$$X(R) = X_0 + \alpha_1 \frac{R}{R_{\rm vir}} + \alpha_2 (\frac{R}{R_{\rm vir}})^2, \quad (1)$$

with best-fitting parameters given in Table 2 for all runs.

On average, the pressure ratio in the core of NCC-like clusters is ∼5–7 per cent, while this is ∼10 per cent in CC-like clusters, while in all cases this ratio settles to ∼10–15 per cent at $R_{\rm vir}$. However, the scatter in the cluster samples is rather large, as shown in Fig. 5 where we show the relation between the cluster mass within R_{500} and the total enclosed CR-to-gas pressure. The data does not show a tight correlation of X with cluster mass or cluster average temperature (not shown), and for every mass bin variations of the ratio in the range $X \sim 10^{-3}$–0.3 can be found. This is at variance with the earlier results by Pinzke & Pfrommer (2010), based on a different numerical methods, where a tight decreasing correlation of X with the host cluster mass is found. The extreme flatness of our profiles is also not in agreement with earlier SPH results (Pfrommer et al. 2007), while it is much more similar to more recent SPH simulations (Pinzke & Pfrommer 2010), indicating that numerical details

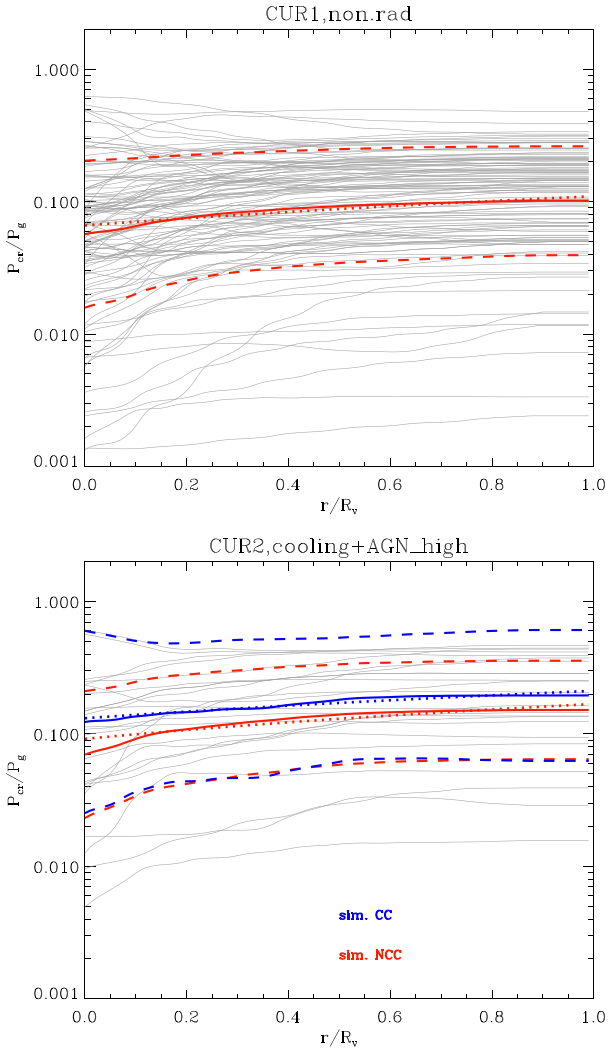

Figure 4. Average radial profile of the CR-to-gas pressure ratio for all simulated clusters in the CUR1 and CUR2 run with cooling and feedback, in all cases for the Kang & Ryu (2013) model of CR acceleration. The grey lines give the profiles of individual clusters while the coloured lines give the mean and the $\pm\sigma$ dispersion. The additional thin coloured line dotted lines give the best fit for the average profiles, with parameters given in Table 2.

Table 2. Best-fitting parameters for the X, R relation for clusters in the CUR1 and CUR2 run, assuming $X(R) = X_0 + \alpha_1(R/R_{\rm vir}) + \alpha_2(R/R_{\rm vir})^2$. In the upper half of the table, we give the best fit for the CC and NCC-like clusters separately, in radiative runs. The lower half of the table gives the best-fitting parameters limited to all $M \geq 10^{14}\,{\rm M}_\odot$ clusters in the CUR2 runs.

Run	X_0	α_1	α_2
CUR1	0.056	0.099	−0.055
CUR2, cool+AGN high (CC)	0.117	0.162	−0.082
CUR2, cool+AGN high (NCC)	0.072	0.198	−0.116
CUR2, cool+AGN low (CC)	0.497	−0.373	−0.192
CUR2, cool+AGN low (NCC)	0.367	−0.030	−0.044
CUR2, non-rad, KJ07	0.094	0.170	−0.113
CUR2, non-rad, KR13	0.068	0.132	−0.084
CUR2, non-rad, 10^{-3}	0.006	0.019	−0.017
CUR2, non-rad, CS14	0.011	0.023	−0.020
CUR2, cool+AGN high, KR13	0.079	0.244	−0.155
CUR2, cool+AGN low, KR13	0.334	−0.012	−0.052
CUR2, cool+AGN high, 10^{-3}	0.025	0.067	−0.038

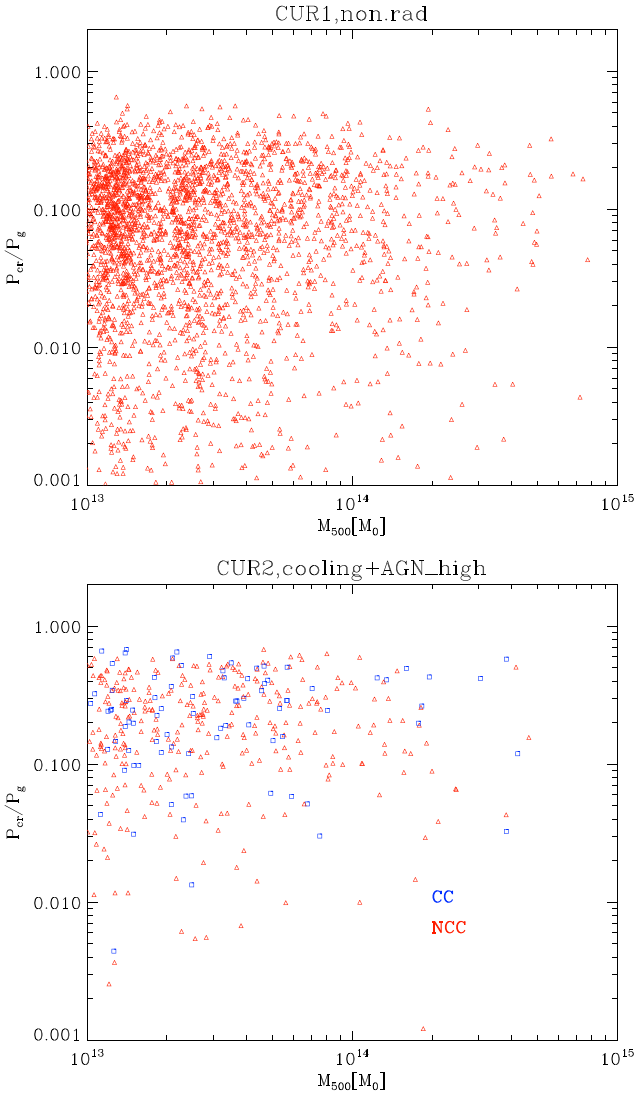

Figure 5. Average enclosed pressure ratio of CR and gas for simulated clusters at $z = 0$. The top panel shows the distribution for the CUR1 run, the bottom panel shows the distribution for the CC- and NCC-like clusters in the CUR2 run with cooling and high-redshift AGN feedback.

play a significant role in the spatial distribution of CRs. We give our interpretation for this comparison in Section 4.

Fig. 6 shows the average profile of CR-to-gas pressure ratio for all $M \geq 10^{14}\,{\rm M}_\odot$ clusters at $z = 0$, where we compare the outcome of the different models for gas and CR physics. The best-fitting parameters in this case are given in the lower half of Table 2. Basically all models predict the same flat shape, with a minimum of $X(R)$ in the cluster core. In this set of models, we also show the case of a *fixed* (re)acceleration efficiency of $\eta = 10^{-3}$ and of the approximated acceleration model we derive from Caprioli & Spitkovsky (2014a). In the $\eta = 10^{-3}$ model both radiative and non-radiative runs also predict a very flat profile outside of clusters core, with a minimum of $X \approx 0.6$ per cent in the non-radiative run and $X \approx 2$ per cent in the cooling and AGN case. The fact that the same fixed acceleration efficiency gives a ∼5 times increased CR-to-gas pressure ratio stresses how much baryon physics can affect the modelling of CRs in the ICM, and the quantitative interpretation of γ-ray data (see Section 3.3). The profiles obtained with the Caprioli

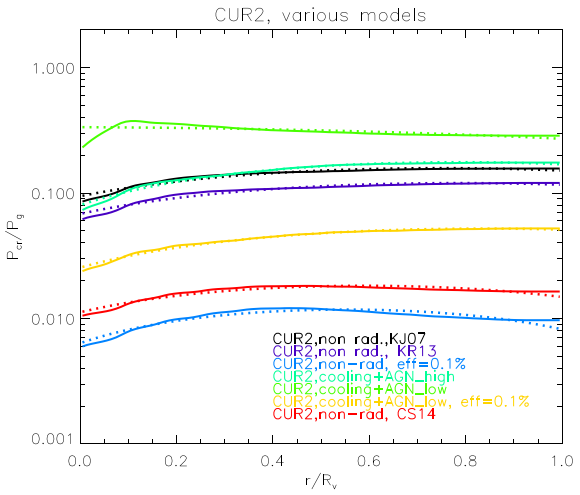

Figure 6. Average profile of $X(R)$ for all $M \geq 10^{14}\,M_{\odot}$ clusters in the CUR2 run, comparing different physical prescriptions for CRs and baryons. The dotted lines give the best-fitting relation for each model, with parameters given in Table 2, whereas the dashed lines give the $\pm 1\sigma$ standard deviations on the average profiles.

& Spitkovsky (2014a) model have a similar shape, with a ∼2 higher normalization.

3.3 Hadronic γ-ray emission from simulated cluster samples

The hadronic emission from the CRs population of each simulated cluster is computed following the standard formalism of Pfrommer & Enßlin (2004) and Donnert et al. (2010), with the only difference that for the hadronic cross-section we use the parametrization of the proton–proton cross-section given by Kelner et al. (2006), as in Huber et al. (2013). A recent review of the method is given in Vazza et al. (2015). Our two-fluid formalism cannot follow particle spectra and therefore we have to guess a fixed spectral energy distribution of CRs in the simulated volumes. We consider here the large 0.2–200 GeV energy range to be less sensitive to the exact spectral energy distribution of CRs, which is not directly simulated in our method. The first panel of Fig. 7 shows the distribution of the predicted emission as a function of the cluster mass for the non-radiative clusters of the CUR1 run, where we computed the hadronic emission from each cluster for the cases of a fixed $s = 2.0$ (corresponding to a γ-ray spectrum of $s_\gamma \approx 2.5$ at high energy[1]) and $s = 3.0$ ($s_\gamma \approx 3.33$). We notice that here we assume slightly steeper spectra compared to Pinzke & Pfrommer (2010), who found nearly universal energy spectra compatible with $s \approx 2.3$ for most of the CR-energy range. In our case, these estimates follow from the distribution of CR-energy injected by merger shocks seen in these simulations (Vazza, Brunetti & Gheller 2009; Vazza et al. 2010, 2011), and are also confirmed by our tracer-based modelling of the following section (Section 3.4). In all cases, considering the large energy range used here to compare with *Fermi* data, the effect of the spectral shape is not big in our predictions and the total photon flux is only varied by a ∼50 per cent going from $s = 2.0$ to 3.0, not a big effect. Our predictions are compared to the observed upper limits from the *Fermi* satellite, within the same energy range, obtaining by converting each limits on the received photon flux into a limit on the absolute luminosity at

[1] s_γ is the spectrum of the γ-ray emission and is given by $s_\gamma = 4(s - 1/2)/3$ (e.g. Pfrommer & Enßlin 2004).

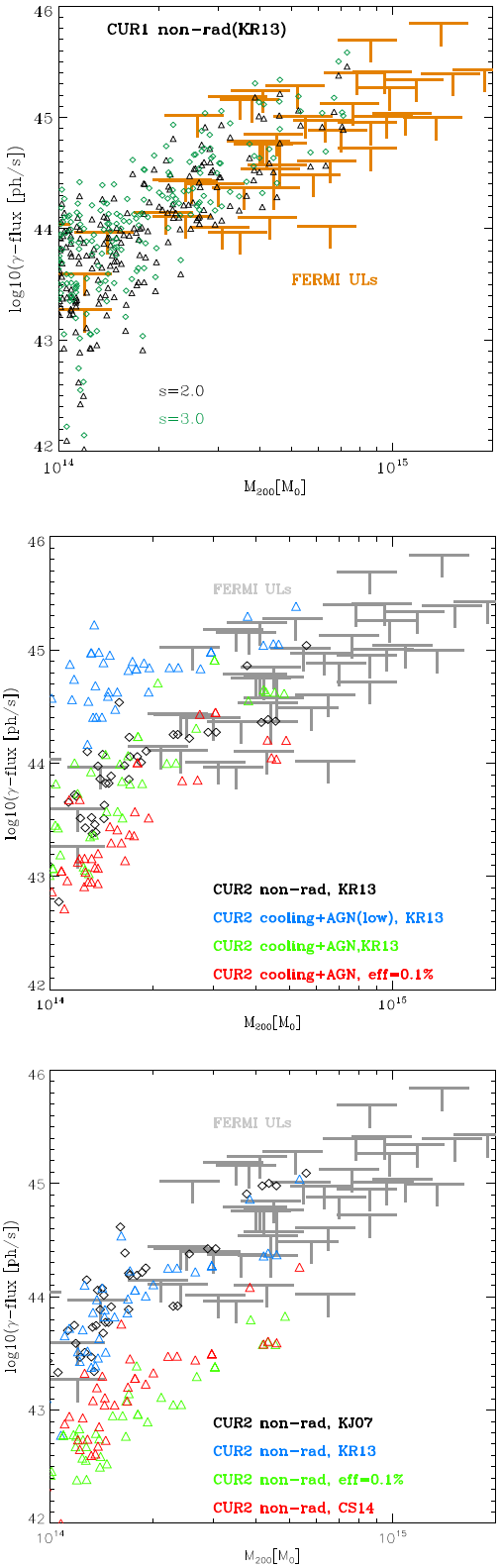

Figure 7. Hadronic emission for our simulated clusters at $z = 0$, in the 0.2–200 GeV energy range. Top panel: γ-emission for clusters in the CUR1 box, assuming CR-spectra of $s = 2.0$ or 3.0. Centre: γ-ray emission from clusters in the CUR2 runs, for different models of gas physics. Bottom: γ-ray emission from clusters in our non-radiative CUR2 run, for runs with different acceleration efficiency of CRs. The grey symbols are the upper limits from the *Fermi* catalogue in the same energy range.

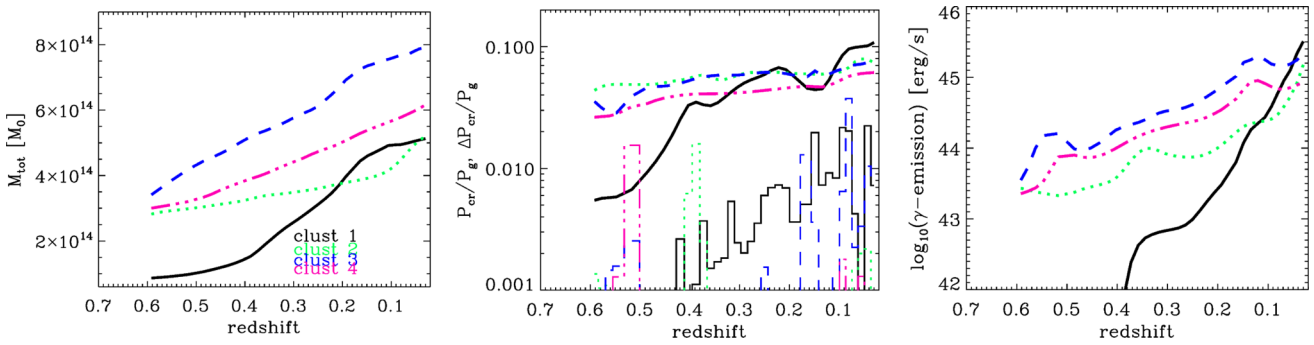

Figure 8. Evolution of four clusters with a final mass $\geq 5 \times 10^{15}\,M_\odot$ in the CUR1 volume. From left to right the image shows: (a) the enclosed total mass with fixed 6^3 Mpc^3 comoving volumes; (b) the total CR-to-gas pressure ratio (thick lines) and the relative CR pressure increment snapshot by snapshot (think lines); (c) the total hadronic γ-ray emission from the same volumes.

the distance of each object. For ∼50 per cent of simulated clusters, the predicted emission is at the level or above the upper limits from *Fermi* observations.

The effect of different prescriptions for gas physics or CR physics is shown in the lower panels of Fig. 7. Radiative feedback worsens the comparison with observations, by producing typically denser gas cores (CUR2 run with low-redshift feedback) or by increasing the number of shocks connected to AGN feedback (CUR2 run with high-redshift feedback). The use of the (higher) acceleration efficiency assumed in Kang & Jones (2007) obviously produces an even higher hadronic flux. The approximated version of the Caprioli & Spitkovsky (2014a) acceleration model significantly reduces the number of objects above *Fermi* limits, but does not entirely solve the problem as still ∼10–20 per cent of simulated objects are above *Fermi* limits. We found that only by limiting the overall acceleration efficiency of shocks to $\eta = 10^{-3}$ for all Mach numbers, the predicted hadronic emission goes below the *Fermi* limits in the non-radiative case, while the fraction of clusters that is inconsistent with *Fermi* limits is now limited to ≤10 per cent in the cooling+AGN feedback case. In the latter case, these high γ-ray emitters are the densest CC-like objects in the volume.

All models vary with mass in that the hadronic emission scales as $\epsilon_\gamma \propto M^{5/3}$, with normalization varying with the physical model and a ∼1–2 dex scatter around the mean relation that increases going to the lowest masses. While the $\propto M^{5/3}$ relation is in line with earlier results by Pfrommer (2008) and Pinzke & Pfrommer (2010),[2] the level of scatter we observe is significantly larger.

To understand the origin of this large scatter, we focus on four clusters in the largest CUR1 box, with large final masses ($\geq 5 \times 10^{14}\,M_\odot$) but different dynamical histories. For each of these objects, we analysed 50 snapshots equally spaced in time from $z = 0.6$ to 0, and extracted the mean properties of gas and CRs within fixed comoving volumes centred on each object. Fig. 8 gives the evolution of the total enclosed mass, of the CR-to-gas pressure ratio (including the CR pressure ratio generated by the injection of CRs over each single snapshot), and of the enclosed γ-ray emission. The evolutionary tracks of these clusters show that the total cluster mass is not the only variable that sets the γ-ray emission, but also the mass accretion rate induces significant scatter on top of the global $\epsilon_\gamma \propto M^{5/3}$ relation. For example, cluster 1 has the final smallest mass in this sample, but the highest hadronic emission at $z = 0$, because it has been rapidly assembled during $z = 0.4$–0.2 in a merger event. This led to an increase of the number of shocks, to enhanced injection of CRs and to a nearly $\sim 10^4$ times increased γ-ray emission from $z = 0.4$ to 0. On the other hand, the hadronic emission of more massive but more relaxed clusters 3 and 4 is only increased by $\sim 10^2$ from $z = 0.6$ to 0. Cluster 2 experiences a major merger late in its evolution ($z \leq 0.1$), which leads to a ∼10 times increase of hadronic emission over the last ∼1.5 Gyr. These different evolutionary paths show that the hadronic emission in our clusters can vary by a few orders of magnitudes during the typical crossing time of clusters, due to the enhanced injection of CRs and due to the gas compression of the ICM during mergers. Cooling and AGN feedback further add a source of scatter to the relation with the host cluster mass. We further elaborate on the variance of our results compared to Pfrommer (2008) and Pinzke & Pfrommer (2010) in Section 4.

3.4 Hadronic γ-ray emission from MACSJ1752

We finally focus on the resimulations of a major merger event leading to X-ray and radio morphologies similar to the observed cluster MACSJ1752.0+0440, which we already studied in Bonafede et al. (2012). Fig. 9 gives the merger sequence ($0.4 \geq z \geq 0.25$) for the simulated cluster, showing the projected X-ray brightness and the radio emission using the formalism by Hoeft & Brüggen (2007). Since the magnetic field is not included in our simulation, we assume that the energy in the magnetic field is everywhere $1/\beta = 1/100$ of the thermal gas energy within the cell, which gives $\sim \mu$G fields in this case. For the electron acceleration efficiency at shocks, we assumed that this is $10^{-3} \times \eta(\mathcal{M})$, where $\eta(\mathcal{M})$ is the acceleration efficiency by Kang & Ryu (2013).

The total virial mass of the system after the collision is $\approx 0.65 \times 10^{15}\,M_\odot$, while the mass ratio of the merger is $M_1/M_2 \sim 1.6$. At $z \sim 0.3$, the shock propagating downstream of the main cluster progenitor has $\mathcal{M} \approx 4.5$ and produces a total radio emission of $P_{\rm radio} \sim 10^{26}$ erg/(s Hz) at 325 MHz over an extent of ∼1.5 Mpc, similar to observations. Downstream of the smaller cluster progenitor, also a second radio relic ∼700 kpc wide and with a total power $P_{\rm radio} \sim 3 \times 10^{25}$ erg (s Hz)$^{-1}$ is formed. The double relic configuration observed in MACSJ1752.0+0440 at $z \approx 0.3$ should be produced ∼0.8 Gyr after the central collision of the cores, and we use this epoch also to constrain the acceleration scenario of CRs based on the lack of γ-ray emission.

[2] The ∼5/3 exponent can be understood if the average CR-to-gas energy ratio is a constant, in which case the total γ-emission scales as the thermal gas energy of the cluster, $\epsilon_\gamma \propto E_{\rm g} \int \gamma n X$, and $E_{\rm g} \propto M^{5/3}$ in virialized clusters (e.g. Vazza et al. 2006).

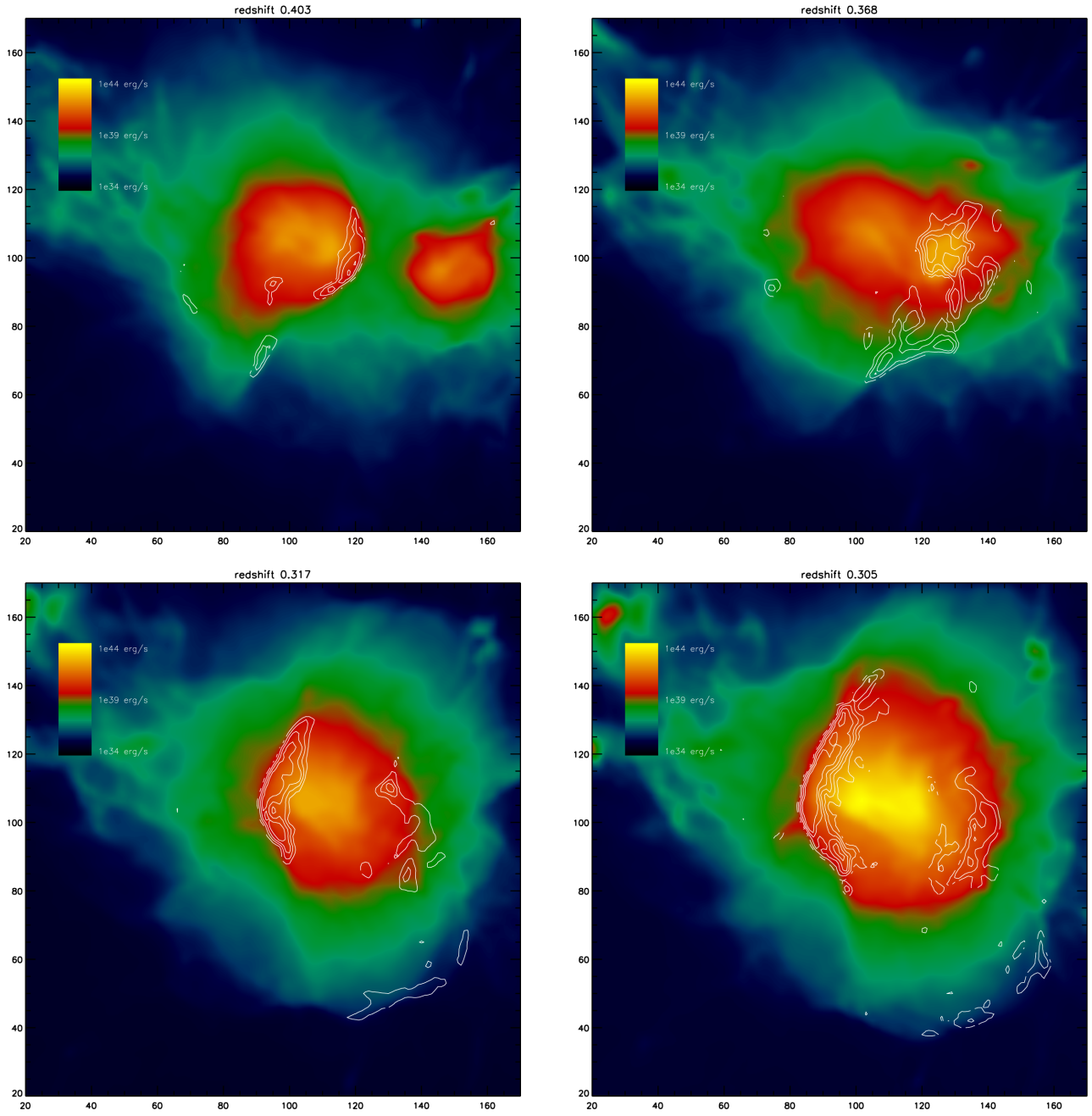

Figure 9. Simulated merger sequence for a $\sim 10^{15}\,M_{\odot}$ cluster using AMR, with X-ray emission in colours and radio emission in white contours. The approximate epoch of the observed merger in MACSJ1752.0+0440 is $z \approx 0.3$. Each image is 5×5 Mpc^2 (comoving) across. The contours are equally spaced with $\sqrt{2}$ multiples of the radio emission, starting from $\approx 10^{23}$ erg (s Hz)$^{-1}$ per pixel.

The evolution of the projected CR-proton energy simulated with our two-fluid method in ENZO is given in Fig. 10, for the Kang & Ryu (2013) injection model. The late energy budget of CRs in the innermost cluster regions is clearly dominated by the injection through the $\mathcal{M} \sim 4$ shock launched by the major merger at $z \approx 0.3$. However, on larger scales the CR-energy mostly results from the cumulative activity of previous formation shocks and can be considered as a background CR-energy distribution present regardless of the last major merger. We notice that, compared to our first study in Bonafede et al. (2012), the effect of the additional CR-pressure in this set of simulations results into a less satisfactory match of the simulated X-ray and radio emission compared to the observation. However, several significant features as the elongated a disrupted inner X-ray structure, the emergence of the double relic and the off-set of the least powerful relic respect to the merger axis are well reproduced. Given that the masses and the relative distances between the gas cores and the relics allow a reasonable reconstruction of the merger scenario, we consider this system an interesting case to test CR acceleration models against the *Fermi* limits for this system (Section 2.4).

While our two-fluid formalism only allows us to monitor the total CR-energy in each cell, with the complementary use of passive tracer particles we can better follow the spatial evolution of CRs in the ICM (e.g. Vazza 2011). To this end, for one AMR run we saved

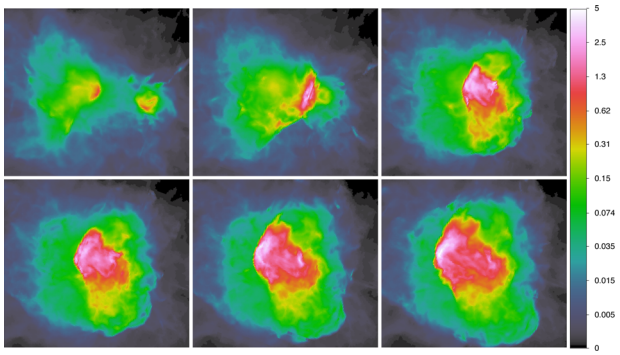

Figure 10. Merger sequence for our simulated versions of the cluster MACSJ1752.0+0440 using AMR for the same area of Fig. 9 and for the epochs of $z = 0.403$, 0.368, 0.317, 0.305, 0.294 and 0.281. The colours show the total projected CR-energy in code units.

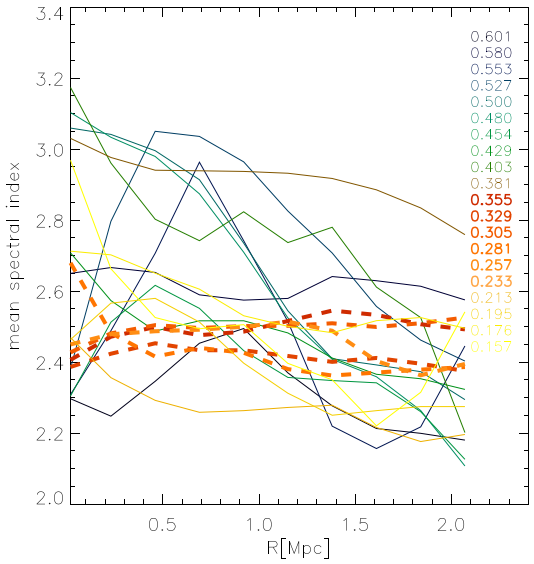

Figure 11. γ-ray emission weighted radial distribution of the spectral index of CR-energy in the AMR resimulation of MACSJ1752 for different redshifts (marked in different colours). The thick dashed lines marked the epochs closer to the observed radio emission.

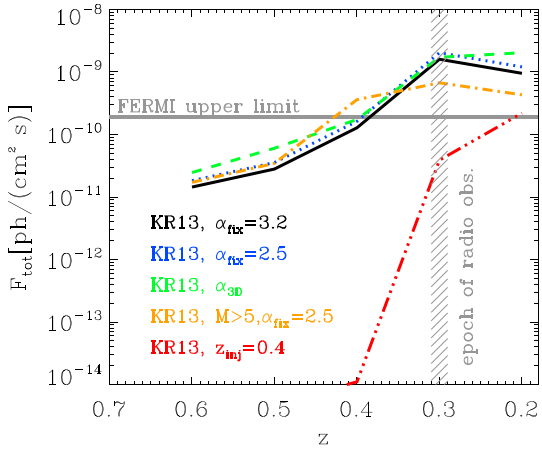

Figure 12. Evolution of the total hadronic γ-ray emission in the 0.2–100 GeV energy range for the various resimulations of cluster MACSJ1752. The vertical hatched region shows the epoch of the observed X-ray/radio configuration, while the horizontal line marks the upper limits from *Fermi* on the hadronic emission from this cluster.

~50 equally time-spaced snapshots from $z = 1$ to 0 and we evolved the trajectory of passive tracers using the output three-dimensional velocity field. The underlying assumption is that CRs can be treated as frozen into the gas as their spatial diffusion is negligible on these scales (~34 kpc). We injected in total $\approx 6 \times 10^6$ tracers at $z = 1$, with initial distribution proportional to the gas density in the ENZO run. Their positions were updated at every time step with explicit time integration and using the same Courant condition of the ENZO simulation. The tracer velocity was computed from the grid values at the tracer position using a CIC interpolation that includes a turbulent correction term to better model the mass flux. For each tracer, we recorded the CR energy read from the grid, and evolved the spectral index of the CR-energy of each tracer integrating over all injected populations of CRs, assuming an injection spectrum of $s = 2(\mathcal{M}^2 + 1)/(\mathcal{M}^2 - 1)$. In the case of multiple shocks hitting a tracer, the final CR-spectrum kept the smallest slope given by the time sequence of shocks (e.g. Kang & Ryu 2010), while the normalization was updated based on the CR-energy, computed from the grid. With this approach, we can monitor the spatial evolution of CR spectra in the cluster and have a better modelling of the resulting γ-ray emission. More details on the tracers algorithm will be given in a forthcoming paper, by Wittor et al. (in preparation).

Fig. 11 shows the average γ-ray emission weighted profile of CR-spectra for this cluster at different redshifts, with the thick dashed lines marking the epochs around the merger event. The average spectrum of CRs is initially steep in the cluster centre, $s \approx 3$ and flatter in the outskirts, $s \approx 2.2$, mirroring the typical distribution of shocks in clusters, which are weaker in the centre and stronger outwards (e.g. Vazza et al. 2011). Later on, with the progress of the merger the spectrum flattens everywhere as the $\mathcal{M} \sim 4$–5 shock sweeps the intracluster volume. At the approximate epoch of the X/radio observation, the average spectrum has a flat distribution around $s \sim 2.4$–2.5, with significant fluctuation patches spread over the cluster volume.

As a final result, the evolution of the predicted γ-ray emission for a few scenarios for CRs is given in Fig. 12. Here, we show the hadronic emission obtained using fixed CR-spectra of $s = 2.5$ or 3.2, or directly using the 3D spectral information from the tracers. Despite fluctuations of the order of ~2–3 in the total emission, the *Fermi* limits derived in Section 2.4 are in all cases exceeded by a factor ~10 at the epoch of the radio observation of MACSJ1752.0+0440. It is not only the major merger that is responsible for the boost of the γ-emission: in an additional run assuming the Kang & Ryu (2013) model, we only allowed the injection/re-acceleration of CRs by $\mathcal{M} \geq 5$ shocks. In this case, the hadronic emission is greatly reduced compared to all previous models, yet the *Fermi* limits are still exceeded by a factor ~2–3 at $z = 0.3$. Finally, as a simple test we rerun the AMR simulation by imposing that the acceleration of particles only begins at $z = 0.4$, i.e. when the major merger begins. The hadronic emission ramps up during the merger, yet the predicted emission at $z = 0.3$ is below the constraints by *Fermi*. This confirms that while the injection of CRs during a merger can significantly boost the hadronic emission from the ICM, the problem of simulated models to fulfil *Fermi* constraints more generally stems from the assumed CR-enrichment across the full structure formation process. Our findings here for MACSJ1752.0+0440 are also consistent with the semi-analytical model we presented in Vazza et al. (2015), where the predicted hadronic emission resulting from the major merger is ~10 per cent of the *Fermi* limit for this object. However, in the case of a few

closer systems with relics such as A3367, ZwCLJ2341, A754 and A2256, the limits by *Fermi* are challenged even by considering the last merger only (see Vazza & Brüggen 2014; Vazza et al. 2015, for more details).

4 DISCUSSION

Both our non-radiative and radiative runs produce galaxy clusters with a budget of CRs in tension with the latest *Fermi* limits (e.g. The Fermi-LAT Collaboration et al. 2014), suggesting the necessity of a revision of the acceleration efficiency from DSA in cosmic shocks. These conclusions are in line with the results of our previous semi-analytical modelling of double relics (Vazza & Brüggen 2014; Vazza et al. 2015) and put typically stronger constraints on the acceleration of CRs by cosmic shocks compared to previous works based on simulations (e.g. Ryu et al. 2003; Kang et al. 2007; Pfrommer et al. 2007; Pinzke & Pfrommer 2010; Vazza et al. 2012, 2013).

We can briefly discuss possible explanations for this finding. First, the real efficiency from diffusive shock (re)acceleration of protons by weak shocks ($\mathcal{M} \leq 5$) is $\sim$10–100 times below the current estimates from DSA. This is reasonable as the latest results of particle-in-cell and hybrid simulation of cosmic shocks are revising downwards the estimates of CR-protons acceleration efficiency (Caprioli & Spitkovsky 2014a; Guo et al. 2014a). Our test based on the Caprioli & Spitkovsky (2014a) acceleration model shows that the tension with *Fermi* is alleviated if the overall DSA acceleration efficiency is revised downwards assuming that only quasi-parallel shocks efficiently accelerate CR-protons, and that the acceleration efficiency is $\sim 1/2$ of what derived in Kang & Ryu (2013). However, in this case the acceleration mechanism in radio relics must be different from DSA, due to the too large electron-to-proton ratio ($K_{e/p} > 10^{-2}$) needed to explain the data (Brunetti & Jones 2014; Vazza & Brüggen 2014; Vazza et al. 2015). The shock-drift-acceleration (SDA) mechanism may indeed lead to this result, as shown by Guo et al. (2014a,b). However, due to computational limitations it was impossible to reach the full *Fermi* I acceleration regime, and therefore the acceleration efficiency of electrons is not yet well constrained in this scenario.

On the other hand, aged relativistic electrons that are reaccelerated by shocks can solve the problem (e.g. Pinzke et al. 2013; Kang & Ryu 2015), but only if the electrons have been injected by leptonic-dominated jets from radio galaxies (or other leptonic scenarios). If instead the aged electrons are assumed to be the result of previous injection by cosmic shocks, the problem is even exacerbated (Vazza & Brüggen 2014; Vazza et al. 2015). In addition, the acceleration efficiency from DSA might be a steep function of the up-stream magnetization level, i.e. for typical intracluster or intergalactic magnetic fields below some given threshold the acceleration efficiency might drop. This would limit the injection of CRs to some fraction of the intracluster volume, where the magnetic field is amplified, and to the fraction of the cosmic time where cosmic magnetic fields have grown enough (e.g. Brüggen et al. 2005; Dolag, Bykov & Diaferio 2008; Widrow et al. 2012; Vazza et al. 2014b). However, assessing the limiting magnetic field needed to produce DSA in these regimes is difficult, also because upstream magnetic fields might be always amplified by a CR-driven dynamo (Drury & Downes 2012; Brüggen 2013; Park, Caprioli & Spitkovsky 2015). While in this work we could only explore the impact of magnetic fields in a very crude way (CS14 model) by assuming they are randomly oriented in space, we defer to future work with MHD simulations (Wittor et al., in preparation) that will exactly address this issue.

Finally, we discuss the main limitations of our modelling and the comparison with the literature.

(i) *Comparison with SPH results.* Our distribution of the CR-to-gas pressure ratio is at variance with SPH (Pinzke & Pfrommer 2010), who found a much tighter relation between the host cluster mass. We find instead that mergers boost the ratio up to $\sim$1–2 orders of magnitude. This is mostly due to the steeper acceleration efficiency model we assume here (Kang & Ryu 2013). For example, our acceleration efficiency goes from $\approx 10^{-5}$ at $\mathcal{M} = 2$ to $\approx 10^{-2}$ at $\mathcal{M} = 3$. On the other hand, in the model by Enßlin et al. (2007) the acceleration efficiency goes from $\approx$0.01 to $\approx$0.2 in the same range of Mach numbers, i.e. their acceleration efficiency is ~ 10–10^2 times larger than ours. Therefore, our model for CRs is more sensitive to the rare $\mathcal{M} \geq 3$ shocks driven by mergers, while in Pinzke & Pfrommer (2010) the injection of CRs is overall more constant over time because also $\mathcal{M} < 3$ shocks inject significant CRs. Additionally, the way in which gas (and the frozen-in CRs) is transported in the central core of clusters simulated with grid and SPH methods is known to be different (e.g. Frenk et al. 1999; Springel 2010; Vazza 2011; Vazza et al. 2011; Sijacki et al. 2012; Schaller et al. 2015) and this can further amplify differences in the budget of CRs in the cluster centre.

(ii) *Comparison with grid results*. Compared to the earlier work by Miniati et al. (2001) and Miniati (2003), we improve on the spatial resolution by $\sim$2–4 times and the total number of simulated clusters by $\sim 10^2$ times. The hydro scheme we applied is also different, and the CRs have a dynamical impact on the gas evolution, while they are passive in Miniati et al. (2001) and Miniati (2003). Our main findings however, including the cluster to cluster scatter, are basically in line with these previous results.

(iii) *Comparison with semi-analytical results.* The results of this work are overall in agreement with our recent modelling of CRs acceleration in double relics using semi-analytical methods (Vazza & Brüggen 2014; Vazza et al. 2015). There we limited our analysis to the (re)acceleration of electrons and protons by the merger shocks which should be responsible for the observed radio emission, and therefore we had to neglect the previous enrichment of CRs during structure formation. Even in this case, we find that overall the acceleration efficiency of protons must be limited to $\leq 10^{-3}$ for the range of Mach numbers inferred by radio spectra, $\mathcal{M} \sim 2-5$.

(iv) *Spatial resolution.* Our spatial resolution is the result of a compromise between the necessary detail on shocks and on the need of sampling large volumes. Earlier works (e.g. Ryu et al. 2003; Skillman et al. 2008; Vazza et al. 2009, 2011) show that a spatial resolution of $\sim 200-300$ kpc is enough to properly resolve the thermalization by cosmic shocks. Our analysis of these simulated volumes (Vazza et al. 2014a) also shows that at the resolution of $\sim 100-200$ kpc the global properties of CRs are converged. Additional resolution tests are given in the appendix.

(v) *Cooling and AGN feedback.* While we do not find a significant *direct* impact of AGN feedback and CR enrichment for the large scales of interest here, the cumulative effect of the cooling-feedback interplay can change the thermodynamical structure of the ICM and affect the CR-to-gas ratio and the γ-ray emission. Modelling AGNs in cosmological simulations is still challenging (Sijacki & Springel 2006; Sijacki, Springel & Haehnelt 2009; Dubois et al. 2010; McCarthy et al. 2010), and so is the complex interplay between AGN injected CRs and the surrounding gas (Aleksić et al. 2012; Pfrommer 2013; Vazza et al. 2013). However, our simulations show that including cooling and feedback *worsens* the comparison with *Fermi* limits. Therefore our main findings on the too large acceleration of

CRs should be conservative against more complex models for the gas physics.

(vi) *Limitations of CR physics*. Our runs do not include all possible interactions between CRs and gas and we assume that CRs do not diffuse neither stream out of the gas distribution. However, in Vazza et al. (2013) we tested that including CR-losses does not affect the distribution of CRs outside of cluster cores, while most of the γ-emission is mostly produced on larger scales. Additional mechanisms of (re)acceleration of CRs, such as turbulent reacceleration (e.g. Brunetti & Jones 2014), reconnection (e.g. Lazarian et al. 2015) and injection by AGN and supernovae (e.g. Völk, Aharonian & Breitschwerdt 1996) can only increase the budget of CRs estimated in our simulations. The spatial diffusion of CRs can modify the distribution simulated by our two-fluid method (Berezinsky et al. 1997). Yet again, this cannot significantly affect our predicted γ-ray emission, which is spread across $\sim$Mpc scales, while the diffusion of $\sim$1$-$10 GeV protons over gigayears can only affect $\sim$10$-$10^2 kpc scales. Finally, the detailed calculation by Wiener, Oh & Guo (2013) showed that even in a scenario in which CRs can stream out of the gas distribution faster than the Alfvén speed, the γ-ray emission is not affected in the energy range probed by *Fermi*, but only at much higher energies (E = 300–1000 GeV).

5 CONCLUSIONS

We simulated the acceleration of CRs by structure formation shocks, and focused on the observable γ-ray outcome of CRs in galaxy clusters. Our suite of simulations has been designed to simulate several realistic scenarios for CRs and gas physics, and to enable the testing for large complete samples of galaxy clusters (Vazza et al. 2014a).

(i) All tested CRs (re)acceleration models based on DSA predict a level of hadronic emission inconsistent with γ-ray observations. A significant fraction of our simulated clusters ($\sim$25–50 per cent depending on the model) produce γ-ray emission above the upper limits reported by *Fermi* (Ackermann et al. 2010, 2014; Huber et al. 2013; The Fermi-LAT Collaboration et al. 2014; Griffin et al. 2014; Zandanel & Ando 2014).This result is robust against the variations in the gas physics that we have tested.

(ii) Regardless of the models (with the exception of the unrealistic gas model producing overcooling within haloes), we find that the average radial profile of CRs to gas pressure, $X(R)$, is well described by a simple second-order polynomial expression (equation 1). In all models the profiles are very flat for $R \geq 0.2R_{\rm vir}$, and have a central normalization X_0 depending on the acceleration model. This average profile can be useful for the inversion of *Fermi* data of clusters (e.g. Ackermann et al. 2014).

(iii) Clusters of similar mass have a total pressure ratio X that varies up to a factor $\sim$10–10^2 depending on their dynamical state. In non-radiative simulations, the main source of scatter is caused by mergers, which inject new CRs and boost the hadronic emission. In radiative simulations, cooling and feedback can also increase the CR-to-gas pressure ratio by lowering the gas temperature and by triggering stronger shocks from the innermost cluster regions of CC-like clusters.

(iv) The different average CR-to-gas pressure ratio in clusters with similar mass, due to their different dynamical history, suggests that the present *Fermi* limits are actually constraining the total budget of CRs in the average cluster population to a deeper level than usually assumed. Indeed, the non-detection of hadronic emission mostly puts a constrain on the budget of CRs in the active systems, which must be limited to $X \sim 1$ per cent to be consistent with *Fermi* limits (Huber et al. 2013; The Fermi-LAT Collaboration et al. 2014; Ackermann et al. 2014; Griffin et al. 2014). However, given the range of scatter in X across our simulated clusters, we conclude that in more relaxed systems this ratio must be even lower, $X \sim$ 0.1 per cent, i.e. nearly 10 times below the average limit given by the modelling of *Fermi* stacking (Huber et al. 2013; The Fermi-LAT Collaboration et al. 2014).

(v) This result suggests that the (re)acceleration efficiency assumed for CRs must be significantly scaled down compared to all models tested here, which are derived from diffusion-convection simulations of DSA (Kang & Jones 2007; Kang & Ryu 2013). Revising the acceleration efficiency by Kang & Ryu (2013) downwards based on the latest results of hybrid simulations by Caprioli & Spitkovsky (2014a) is found to limit the tension with *Fermi* data to a few objects. A *fixed* proton (re)acceleration efficiency $\eta = 10^{-3}$ at all shocks produces hadronic emission from clusters below the present upper limits from *Fermi*. In this case, the central CR-to-gas pressure ratio is $\approx$0.6 per cent and reaches 1 per cent within the virial radius. The energetics of CRs in clusters is largely dominated by $\mathcal{M} \sim 2-5$ shocks, this turns into a requirement for the acceleration efficiency in this Mach number range. However, also the acceleration efficiency by stronger external shocks (usually assumed in the range $\eta \sim 10$ per cent) must be revised, as our test in Section 3.4 shows. This result is in agreement with the independent modelling based on semi-analytical mergers discussed in Vazza et al. (2015), where also a $\sim 10^{-3}$ acceleration efficiency of protons at shocks was found to be necessary to reconcile with the lack of detected hadronic emission from clusters hosting radio relics.

(vi) These results strengthen the problems we pointed out in a related series of semi-analytical paper focusing on double relics (Vazza & Brüggen 2014; Vazza et al. 2015), where we reported that in order to reconcile the shock-acceleration model of relics with the absence of γ-ray emission from protons, a electron-to-proton injection ratio ($\gg 10^{-2}$) larger than canonic DSA must be assumed. A promising solution to this problem might come from the latest work on particle acceleration given by particle-in-cell simulations (Guo et al. 2014a,b), which found efficient pre-acceleration of relativistic electrons and very little proton injection by $\mathcal{M} \leq 5$ shocks, due to SDA. In addition, hybrid (Caprioli & Spitkovsky 2014a,b) or PIC (Park et al. 2015) simulations of proton acceleration by stronger shocks reported large variations of the injected CR-energy depending on the shock obliquity with the upstream magnetic field.

In conclusion, this study shows that cosmological simulations joined with γ-ray observations can be used as a laboratory to study the acceleration of CRs by weak cosmic shocks, in a regime complementary to supernova remnants and solar wind shocks.

ACKNOWLEDGEMENTS

This work was strongly supported by computing resources from the Swiss National Supercomputing Centre (CSCS) under projects ID ch2 and s585 in 2014–2015. FV acknowledges personal support from the grant VA 876/3-1 from the Deutsche Forschungsgemeinschaft. FV and MB also acknowledge partial support from the grant FOR1254 from the Deutsche Forschungsgemeinschaft. We acknowledge the use of computing resources under allocations no. 7006 and 9016 (FV) and 9059 (MB) on supercomputers at the NIC of the Forschungszentrum Jülich. We acknowledge the use of the online 'Cosmology Calculator' by Wright (2006). We thank K.

Dolag for very fruitful discussions at an early stage of this work, and our referee H. Kang for very useful comments on the manuscript.

REFERENCES

Ackermann M. et al., 2010, ApJ, 717, L71
Ackermann M. et al., 2014, ApJ, 787, 18
Aharonian F. et al., 2009, A&A, 495, 27
Aleksić J. et al., 2010, ApJ, 710, 634
Aleksić J. et al., 2012, A&A, 541, A99
Arlen T. et al., 2012, ApJ, 757, 123
Berezinsky V. S., Blasi P., Ptuskin V. S., 1997, ApJ, 487, 529
Blasi P., Colafrancesco S., 1999, Astropart. Phys., 122, 169
Bonafede A. et al., 2012, MNRAS, 426, 40
Brüggen M., 2013, MNRAS, 436, 294
Brüggen M., Ruszkowski M., Simionescu A., Hoeft M., Dalla Vecchia C., 2005, ApJ, 631, L21
Brunetti G., Jones T. W., 2014, Int. J. Mod. Phys. D, 23, 1430007
Bryan G. L. et al., 2014, ApJS, 211, 19
Caprioli D., 2012, .J. Cosmol. Astropart. Phys., 7, 38
Caprioli D., Spitkovsky A., 2014a, ApJ, 783, 91
Caprioli D., Spitkovsky A., 2014b, ApJ, 794, 46
Cavagnolo K. W., Donahue M., Voit G. M., Sun M., 2009, ApJS, 182, 12
Cavaliere A., Lapi A., 2013, Phys. Rep., 533, 69
De Grandi S., Molendi S., 2001, ApJ, 551, 153
Dennison B., 1980, ApJ, 239, L93
Dolag K., Bykov A. M., Diaferio A., 2008, Space Sci. Rev., 134, 311
Donnert J., Dolag K., Cassano R., Brunetti G., 2010, MNRAS, 407, 1565
Drury L. O., Downes T. P., 2012, MNRAS, 427, 2308
Dubois Y., Devriendt J., Slyz A., Teyssier R., 2010, MNRAS, 409, 985
Eckert D. et al., 2012, A&A, 541, A57
Eckert D., Molendi S., Vazza F., Ettori S., Paltani S., 2013, A&A, 551, A22
Eckmiller H. J., Hudson D. S., Reiprich T. H., 2011, A&A, 535, A105
Ensslin T. A., Biermann P. L., Klein U., Kohle S., 1998, A&A, 332, 395
Enßlin T. A., Pfrommer C., Springel V., Jubelgas M., 2007, A&A, 473, 41
Feretti L., Giovannini G., Govoni F., Murgia M., 2012, A&AR, 20, 54
Ferland G. J., Korista K. T., Verner D. A., Ferguson J. W., Kingdon J. B., Verner E. M., 1998, PASP, 110, 761
Ferrari C., Govoni F., Schindler S., Bykov A. M., Rephaeli Y., 2008, Space Sci. Rev., 134, 93
Frenk C. S. et al., 1999, ApJ, 525, 554
Gabici S., Blasi P., 2003, ApJ, 583, 695
Griffin R. D., Dai X., Kochanek C. S., 2014, ApJ, 795, L21
Guo F., Oh S. P., 2008, MNRAS, 384, 251
Guo X., Sironi L., Narayan R., 2014a, ApJ, 794, 153
Guo X., Sironi L., Narayan R., 2014b, ApJ, 797, 47
Haardt F., Madau P., 1996, ApJ, 461, 20
Hahn O., Martizzi D., Wu H.-Y., Evrard A. E., Teyssier R., Wechsler R. H., 2015, preprint (arXiv:1509.04289)
Hoeft M., Brüggen M., 2007, MNRAS, 375, 77
Hong S. E., Ryu D., Kang H., Cen R., 2014, ApJ, 785, 133
Huber B., Farnier C., Manalaysay A., Straumann U., Walter R., 2012, A&A, 547, A102
Huber B., Tchernin C., Eckert D., Farnier C., Manalaysay A., Straumann U., Walter R., 2013, A&A, 560, A64
Hudson D. S., Mittal R., Reiprich T. H., Nulsen P. E. J., Andernach H., Sarazin C. L., 2010, A&A, 513, A37
Kang H., Jones T. W., 2007, Astropart. Phys., 28, 232
Kang H., Ryu D., 2010, ApJ, 721, 886
Kang H., Ryu D., 2013, ApJ, 764, 95
Kang H., Ryu D., 2015, ApJ, 809, 186
Kang H., Ryu D., Cen R., Ostriker J. P., 2007, ApJ, 669, 729
Kang H., Ryu D., Jones T. W., 2012, ApJ, 756, 97
Kelner S. R., Aharonian F. A., Bugayov V. V., 2006, Phys. Rev. D, 74, 034018
Komatsu E. et al., 2011, ApJS, 192, 18
Lazarian A., Eyink G. L., Vishniac E. T., Kowal G., 2015, in Lazarian A., de Gouveia Dal Pino E. M., Melioli C., eds, Astrophysics and Space Science Library, Vol. 407, Magnetic Fields in Diffuse Media. Springer-Verlag, Berlin, p. 311
McCarthy I. G. et al., 2010, MNRAS, 406, 822
Miniati F., 2003, MNRAS, 342, 1009
Miniati F., Ryu D., Kang H., Jones T. W., Cen R., Ostriker J. P., 2000, ApJ, 542, 608
Miniati F., Jones T. W., Kang H., Ryu D., 2001, ApJ, 562, 233
Park J., Caprioli D., Spitkovsky A., 2015, Phys. Rev. Lett., 114, 085003
Pfrommer C., 2008, MNRAS, 385, 1242
Pfrommer C., 2013, ApJ, 779, 10
Pfrommer C., Enßlin T. A., 2004, A&A, 413, 17
Pfrommer C., Enßlin T. A., Springel V., Jubelgas M., Dolag K., 2007, MNRAS, 378, 385
Pinzke A., Pfrommer C., 2010, MNRAS, 409, 449
Pinzke A., Oh S. P., Pfrommer C., 2013, MNRAS, 435, 1061
Planck Collaboration V, 2013, A&A, 550, A131
Planelles S., Quilis V., 2013, MNRAS, 428, 1643
Rasia E. et al., 2015, ApJ, 813, L17
Reichert A., Böhringer H., Fassbender R., Mühlegger M., 2011, A&A, 535, A4
Ryu D., Kang H., Hallman E., Jones T. W., 2003, ApJ, 593, 599
Schaller M., Dalla Vecchia C., Schaye J., Bower R. G., Theuns T., Crain R. A., Furlong M., McCarthy I. G., 2015, MNRAS, 454, 2277
Sijacki D., Springel V., 2006, MNRAS, 366, 397
Sijacki D., Springel V., Haehnelt M. G., 2009, MNRAS, 400, 100
Sijacki D., Vogelsberger M., Kereš D., Springel V., Hernquist L., 2012, MNRAS, 424, 2999
Skillman S. W., O'Shea B. W., Hallman E. J., Burns J. O., Norman M. L., 2008, ApJ, 689, 1063
Skillman S. W., Xu H., Hallman E. J., O'Shea B. W., Burns J. O., Li H., Collins D. C., Norman M. L., 2013, ApJ, 765, 21
Smith R. K., Brickhouse N. S., Liedahl D. A., Raymond J. C., 2001, ApJ, 556, L91
Smith B. D., Hallman E. J., Shull J. M., O'Shea B. W., 2011, ApJ, 731, 6
Springel V., 2010, MNRAS, 401, 791
Sunyaev R. A., Zeldovich Y. B., 1972, A&A, 20, 189
The Fermi-LAT Collaboration et al., 2014, ApJ, 787, 18A
van Weeren R. J., Röttgering H. J. A., Brüggen M., Hoeft M., 2010, Science, 330, 347
Vazza F., 2011, MNRAS, 410, 461
Vazza F., Brüggen M., 2014, MNRAS, 437, 2291
Vazza F., Tormen G., Cassano R., Brunetti G., Dolag K., 2006, MNRAS, 369, L14
Vazza F., Brunetti G., Gheller C., 2009, MNRAS, 395, 1333
Vazza F., Brunetti G., Gheller C., Brunino R., 2010, New Astron., 15, 695
Vazza F., Dolag K., Ryu D., Brunetti G., Gheller C., Kang H., Pfrommer C., 2011, MNRAS, 418, 960
Vazza F., Brüggen M., Gheller C., Brunetti G., 2012, MNRAS, 421, 3375
Vazza F., Brüggen M., Gheller C., 2013, MNRAS, 428, 2366
Vazza F., Gheller C., Brüggen M., 2014a, MNRAS, 439, 2662
Vazza F., Brüggen M., Gheller C., Wang P., 2014b, MNRAS, 445, 3706
Vazza F., Eckert D., Brueggen M., Huber B., 2015, MNRAS, 451, 2198
Völk H. J., Aharonian F. A., Breitschwerdt D., 1996, Space Sci. Rev., 75, 279
Widrow L. M., Ryu D., Schleicher D., Subramanian K., Tsagas C. G., Treumann R. A., 2012, SSRv, 166, 37
Wiener J., Oh S. P., Guo F., 2013, MNRAS, 434, 2209
Wright E. L., 2006, PASP, 118, 1711
Zandanel F., Ando S., 2014, MNRAS, 440, 663

APPENDIX A: EFFECTS OF RESOLUTION AND ADDITIONAL PHYSICS

We use the smallest simulated volume in our suite of simulation (CUR3, with side 75 Mpc; see Vazza et al. 2014a) to compare

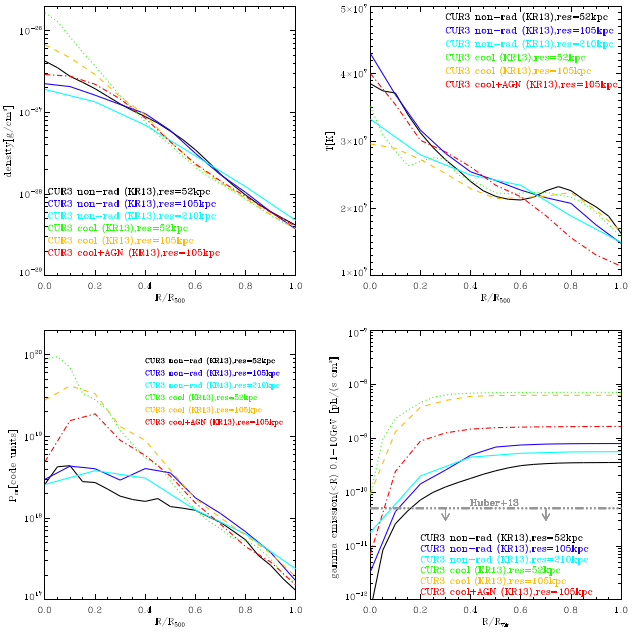

Figure A1. Radial profiles of gas density, gas temperature, CR-pressure and γ-ray emission inside the radius for a $\sim 2 \times 10^{14}\,M_{\odot}$ simulated cluster at $z = 0$, for different resolutions and physical prescriptions for baryons (see the text). The additional horizontal line in the last panel marks the upper limit on the γ-ray emission for the stacking of clusters obtained by Huber et al. (2013).

the effects of resolutions and different physical prescriptions for baryon physics on to the radial distribution of baryons and CRs. Fig. A1 shows the radial profiles of gas density, gas temperature, CR-pressure and γ-ray emission for the most massive halo formed in this box, a cluster with a total mass of $\sim 2 \times 10^{14}\,M_{\odot}$ in a fairly relaxed dynamical state at $z = 0$. We compare here two sets of data: (a) non-radiative runs using the acceleration efficiency of Kang & Ryu (2013) for CRs, and increasing spatial resolution from 210 to 52.5 kpc (i.e. from the number of cells/DM particles in the full volume goes from 256^3 to 1024^3); (b) runs including equilibrium gas cooling and high redshift-AGN feedback, as the main article (see Vazza et al. 2014a, for details), at the resolution of 52.5 and 105 kpc. The trends which are most relevant for the main findings of our article are the effects of resolution/physics in the spatial distribution of gas and CRs in the innermost cluster regions. The most significant differences connected to resolution and gas physics are limited to the innermost $\leq 0.3 R_{500}$ region, where the gas density is increased at most by $\sim$10 times when cooling is not contrasted by AGN feedback, which also appears as a drop in the gas temperature in these runs. The outcome in the CR-pressure is also limited to the innermost region, where radiative runs without AGN feedback present a strong peak in the core, which also corresponds to a $\sim$10 times larger total γ-ray emission. When AGN feedback is applied, the γ-ray emission is only a factor $\sim$2 above the prediction from non-radiative runs at the same resolution. The last panel of

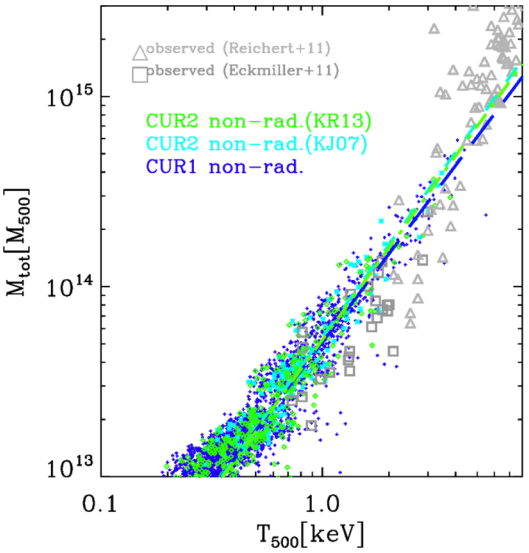

Figure B1. Mass–temperature scaling relation for the haloes in the CUR1 and CUR2 volumes at $z = 0$, where the effect of the Kang & Jones (2007) and Kang & Ryu (2013) acceleration model for CRs are compared. The additional lines show the best fit of the simulated data, while the two set of grey symbols are for real cluster observations using *Chandra* by Eckmiller et al. (2011) and Reichert et al. (2011). To better compare with the simulated cluster and minimize the effect of cosmic evolution, we only consider observed cluster in the $0 \leq z \leq 0.2$ redshift range.

Fig. A1 shows indeed that the hadronic emission is mostly produced at $\geq$0.3–0.4R_{500}, where the differences played by resolution and gas physics are small. In all cases, the predicted hadronic emission for this cluster is larger than the upper limits set by *Fermi* (e.g. Huber et al. 2013). These tests confirm that the problems in explaining the unseen population of CRs in galaxy clusters, outlined in our main article, are robust against variations in resolution and prescriptions for gas physics.

APPENDIX B: IMPACT OF CR PHYSICS ON CLUSTER SCALING RELATIONS

Fig. B1 shows the (M, T) scaling relation within R_{500} for all haloes in the non-radiatie CUR1 run (300^3 Mpc^3) and in the non-radiative CUR2 runs (150^3 Mpc^3) volume, where the impact on the different acceleration models (Kang & Jones 2007; Kang & Ryu 2013) are compared. For the typical pressure ratio between CRs and gas of these runs ($\leq$10 per cent), the dynamical impact of CRs is not enough to cause any significant departures from the self-similar scaling in the $M \propto T^{3/2}$, nor to affect the mass-function of haloes (not shown). In addition, the impact of CRs on the global scaling relation is the same also when more massive clusters (as in the CUR1 run) are included.

This paper has been typeset from a TEX/LATEX file prepared by the author.